energies

MDPI

Article

Mg_6MnO_8 as a Magnesium-Ion Battery Material: Defects, Dopants and Mg-Ion Transport

Navaratnarajah Kuganathan [1,2,*], Evangelos I. Gkanas [2] and Alexander Chroneos [1,2]

1 Department of Materials, Imperial College London, London SW7 2AZ, UK
2 Faculty of Engineering, Environment and Computing, Coventry University, Priory Street, Coventry CV1 5FB, UK
* Correspondence: n.kuganathan@imperial.ac.uk or ad0636@coventry.ac.uk

Received: 8 August 2019; Accepted: 19 August 2019; Published: 21 August 2019

check for updates

Abstract: Rechargeable magnesium ion batteries have recently received considerable attention as an alternative to Li- or Na-ion batteries. Understanding defects and ion transport is a key step in designing high performance electrode materials for Mg-ion batteries. Here we present a classical potential-based atomistic simulation study of defects, dopants and Mg-ion transport in Mg_6MnO_8. The formation of the Mg–Mn anti-site defect cluster is calculated to be the lowest energy process (1.73 eV/defect). The Mg Frenkel is calculated to be the second most favourable intrinsic defect and its formation energy is 2.84 eV/defect. A three-dimensional long-range Mg-ion migration path with overall activation energy of 0.82 eV is observed, suggesting that the diffusion of Mg-ions in this material is moderate. Substitutional doping of Ga on the Mn site can increase the capacity of this material in the form of Mg interstitials. The most energetically favourable isovalent dopant for Mg is found to be Fe. Interestingly, Si and Ge exhibit exoergic solution enthalpy for doping on the Mn site, requiring experimental verification.

Keywords: Mg_6MnO_8; defects; Mg-ion diffusion; dopants

1. Introduction

Rechargeable batteries based on divalent metals such as magnesium, calcium and zinc are being considered as alternatives to Li-ion and Na-ion batteries as they exhibit higher volumetric capacity and redox reactions (more than one electron) [1–3]. Among these, Mg-ion battery technology has attracted significant attention due to the high abundance of Mg, the stability of Mg in the atmosphere and the higher melting point of Mg as compared to Li, ensuring that Mg is safer relative to Li [4–7].

Development of novel cathode materials for Mg-ion batteries is a key challenge as the diffusivity of Mg^{2+} ions is slower in solid state cathode materials due to the strong ionic interaction of Mg^{2+} ions with surrounding anions. The low diffusivity results in poor reversible capacity, high voltage hysteresis and low power output. Owing to the difficulty of Mg^{2+} intercalation, a limited number of electrode materials such as $MgMSiO_4$ (M = Fe, Co and Mn) [8–10], $Mg_xV_2O_5$ [11], $MgFePO_4F$ [12], spinel sulphides [13], molybdenum chalcogenides [14,15], $MgCo_2O_4$ [16] and "Chevrel" $Mg_2Mo_6O_8$ [15] have been reported in the literature.

"Defective rock salt phase" Mg_6MnO_8 has been recently proposed as a potential cathode material for rechargeable Mg-ion batteries, as this material shows a number of advantages including six Mg atoms in a formula unit, low-toxicity, high abundance and ease of preparing the pure phase of this material via solid state reactions [17]. In order to examine the applicability of Mg_6MnO_8, in Mg-ion batteries, Lee et al. [17] used experimental nuclear magnetic resonance (NMR) spectroscopy together with density functional theory (DFT) calculations to characterise the local structure and study the magnetic property of Mg_6MnO_8. Though further electrochemical study by this experimental group is under way, there are no other experimental reports available in the literature.

Fundamental understanding of Mg_6MnO_8 can be useful to optimize the performance of this material. This can be achieved by performing calculations with the aid of well-established atomistic simulations based on the classical pair-wise potentials. The main aim of the present work is to provide valuable information to the experimentalist about defect chemistry and diffusion in Mg_6MnO_8. In previous studies [18–37], this simulation technique has been successfully applied to a number of ionic solids including battery materials. Here, we examine defects, Mg-ion diffusion paths together with activation energies, and favourable dopants on the Mg and Mn site.

2. Computational Methods

Classical pair-wise potential based calculations were performed to examine the most favourable intrinsic defect, possible long-range Mg-ion migration paths with activation energies, and solution enthalpies of isovalent and aliovalent dopants. The GULP code [38] was used. This code uses long-range and short-range forces between ions. The latter arises from electron–electron repulsion and van der Waals attractive forces. The latter was modelled using the Buckingham potentials (Supplementary Materials Table S1). The Broyden–Fletcher–Goldfarb–Shanno (BFGS) algorithm [39] was used to relax the ion positions together with the lattice parameters. Defect modelling was performed using the Mott–Littleton method [40]. This method has been well described in our previous work [18–21]. As the current simulation is based on the full ionic charge model with dilute limit, the defect enthalpies are expected to overestimate. However, the trend would be the same.

3. Results

3.1. Crystal Structure of Mg_6MnO_8

The crystal structure of Mg_6MnO_8 (lattice parameters a = b = c = 8.3818Å and $\alpha = \beta = \gamma = 90°$) was reported by Taguchi et al. [41]. This structure is considered a defect rock salt phase with $Fm\overline{3}m$ space group symmetry. Both Mg^{2+} and Mn^{4+} ions form six bonds with six adjacent O^{2-} ions forming octahedrons (refer to Figure 1). The quality of the classical potentials used in this study (refer to Supplementary Materials Table S1) was validated by performing geometry optimization of bulk Mg_6MnO_8 under constant pressure and comparing the calculated lattice parameters with the corresponding experimental values. The present simulation accurately reproduced the experimental lattice parameters with an error percentage less than 0.6% (refer to Table 1).

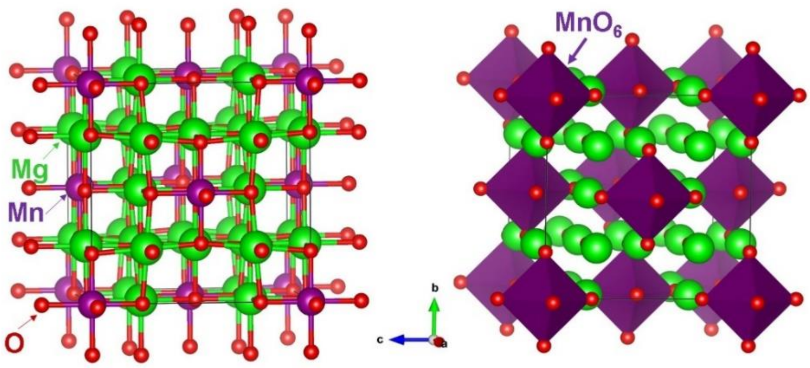

Figure 1. Crystallographic structure of Mg_6MnO_8 (space group $Fm\overline{3}m$).

Table 1. Comparison between the experimental and calculated structural parameters of cubic $\left(Fm\bar{3}m\right)$ Mg_6MnO_8.

Parameter	Calc	Expt[41]	|Δ| (%)
a = b = c (Å)	8.4259	8.3818	0.53
α = β = γ (°)	90.0000	90.0000	0.00
V (Å^3)	598.21	588.86	1.59

3.2. Intrinsic Defect Processes

Isolated point defect energies (vacancies and interstitials) are useful in calculating Frenkel and Schottky reaction energies in Mg_6MnO_8. These energetics provide valuable information about the electrochemical behaviour of Mg_6MnO_8. The following equations (Equations (1)–(8)), written using the Kröger–Vink notation [42], demonstrate the intrinsic defect processes.

$$\text{Mg Frenkel}: \ \mathrm{Mg}_{\mathrm{Mg}}^{X} \rightarrow V_{\mathrm{Mg}}^{\prime\prime} + \mathrm{Mg}_{\mathrm{i}}^{\bullet\bullet} \quad (1)$$

$$\text{O Frenkel}: \ \mathrm{O}_{\mathrm{O}}^{X} \rightarrow V_{\mathrm{O}}^{\bullet\bullet} + \mathrm{O}_{\mathrm{i}}^{\prime\prime} \quad (2)$$

$$\text{Mn Frenkel}: \ V_{\mathrm{Mn}}^{X} \rightarrow V_{\mathrm{Mn}}^{\prime\prime\prime\prime} + \mathrm{Mn}_{\mathrm{i}}^{\bullet\bullet\bullet\bullet} \quad (3)$$

$$\text{Schottky}: \ 6\,\mathrm{Mg}_{\mathrm{Mg}}^{X} + \mathrm{Mn}_{\mathrm{Mn}}^{X} + 8\,\mathrm{O}_{\mathrm{O}}^{X} \rightarrow 6\,V_{\mathrm{Mg}}^{\prime\prime} + V_{\mathrm{Mn}}^{\prime\prime\prime\prime} + 8\,V_{\mathrm{O}}^{\bullet\bullet} + \mathrm{Mg_6MnO_8} \quad (4)$$

$$\text{MgO Schottky}: \ \mathrm{Mg}_{\mathrm{Mg}}^{X} + \mathrm{O}_{\mathrm{O}}^{X} \rightarrow V_{\mathrm{Mg}}^{\prime\prime} + V_{\mathrm{O}}^{\bullet\bullet} + \mathrm{MgO} \quad (5)$$

$$\mathrm{MnO_2}\ \text{Schottky}: \ \mathrm{Mn}_{\mathrm{Mn}}^{X} + 2\,\mathrm{O}_{\mathrm{O}}^{X} \rightarrow V_{\mathrm{Mn}}^{\prime\prime\prime\prime} + 2\,V_{\mathrm{O}}^{\bullet\bullet} + \mathrm{MnO_2} \quad (6)$$

$$\text{Mg/Mn antisite (isolated)}: \ \mathrm{Mg}_{\mathrm{Mg}}^{X} + \mathrm{Mn}_{\mathrm{Mn}}^{X} \rightarrow \mathrm{Mg}_{\mathrm{Mn}}^{\prime\prime} + \mathrm{Mn}_{\mathrm{Mg}}^{\bullet\bullet} \quad (7)$$

$$\text{Mg/Mn antisite (cluster)}: \ \mathrm{Mg}_{\mathrm{Mg}}^{X} + \mathrm{Mn}_{\mathrm{Mn}}^{X} \rightarrow \left\{\mathrm{Mg}_{\mathrm{Mn}}^{\prime\prime} : \mathrm{Mn}_{\mathrm{Mg}}^{\bullet\bullet}\right\}^{X} \quad (8)$$

The calculated reaction energies are reported in Figure 2 (also refer to Supplementary Materials Table S2). Supplementary Materials Table S3 reports the formulas used to calculate the energies of the defect processes. The calculations show that the formation of the anti-site cluster $\left\{\mathrm{Mg}_{\mathrm{Mn}}^{\prime\prime} : \mathrm{Mn}_{\mathrm{Mg}}^{\bullet\bullet}\right\}^{X}$ is the energetically lowest process (1.73 eV/defect). This indicates that the experimental structure consists of both $\mathrm{Mg}_{\mathrm{Mn}}^{\prime\prime}$ and $\mathrm{Mn}_{\mathrm{Mg}}^{\bullet\bullet}$ defects at the same time in the form of a cluster at high temperatures. We considered both defects independently (isolated) and the combined energies. This process (Equation (7)) requires 2.83 eV/defect. The energy difference between the cluster and the isolated form is −1.36 eV. This exoergic energy is essentially the binding energy of isolated defects. This further suggests that the isolated defects are not stable and they would combine to form a cluster. In previous experimental and theoretical studies, this type of defect was observed in a variety of materials, including Li-, Na- and Mg-ion battery materials [18,29,30,35,43–47]. The Mg Frankel was calculated to be the second lowest defect energy process (2.84 eV/defect). This process is important for the vacancy-mediated Mg diffusion in Mg_6MnO_8. This defect is observed at high temperatures as it exhibits endoergic reaction energy. The other Frenkel and Schottky defect processes exhibit high formation energies, suggesting that they cannot be observed at operating temperatures. We considered the loss of MgO in this material by calculating the MgO Schottky process (Equation (5)). In this process, $V_{\mathrm{Mg}}^{\prime\prime}$ and $V_{O}^{\bullet\bullet}$ defects are formed in the lattice. The reaction energy for this process is 3.96 eV per defect, meaning that the loss of MgO is difficult at operating temperatures.

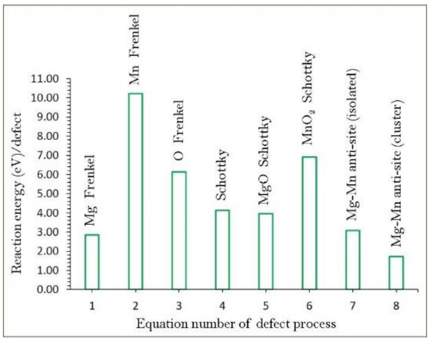

Figure 2. Calculated intrinsic defect energies in Mg_6MnO_8.

3.3. Mg-Ion Diffusion

The mobility of Mg-ions with low activation energies makes battery materials promising. Determination of Mg-ion paths by experiment is often difficult. The current simulation can provide useful information about migration paths and their activation energies. In a previous work, we used this methodology to identify diffusion paths and activation energies for a variety of Li- and Na-ion battery materials [18–37]. Using classical potential simulation, the Li-ion migration path and activation energy were calculated in $LiFePO_4$ by Fisher et al. [48]. The calculated one-dimensional path along the [010] direction was later observed precisely in the neutron diffraction experiment [49].

In Mg_6MnO_8, two Mg–Mg local hops were identified. The first Mg–Mg hop (A) has a distance of 2.98 Å and its corresponding activation energy is 0.82 eV (refer to Figure 3). In the second hop (B), Mg diffuses with a jump distance of 5.96 Å and activation energy of 3.72 eV. Table 2 reports the Mg–Mg separations and their activation energies. Figure 4 shows the energy profile diagrams for local hops A and B. These two local hops were connected to construct three-dimensional migration paths. Three different long range paths were identified (refer to Table 3). In the first long range path (A→A→A→A), Mg-ion diffuses in three-dimensional direction (refer to Figure 3). Its overall activation energy is 0.82 eV. This indicates that Mg-ion diffusion in Mg_6MnO_8 is moderately fast. In the second path (B→B→B→B), Mg-ion migrates along the *ac* plane. The overall activation energy is 3.72 eV meaning that Mg-ion diffusion along this path is unlikely to occur. The third three-dimensional path (A→B→B→A) consists of both local hops A and B, and its overall activation energy is 3.72 eV. As mentioned earlier, the strong ionic interaction of Mg^{2+} ions with adjacent oxygen ions reduces its mobility in the lattice. Several approaches, such as reducing the diffusion distance length of Mg^{2+} ions by synthesising nanostructure materials and decreasing the charge shielding of Mg^{2+} ions, have been made to improve the mobility of Mg^{2+} ions [50,51].

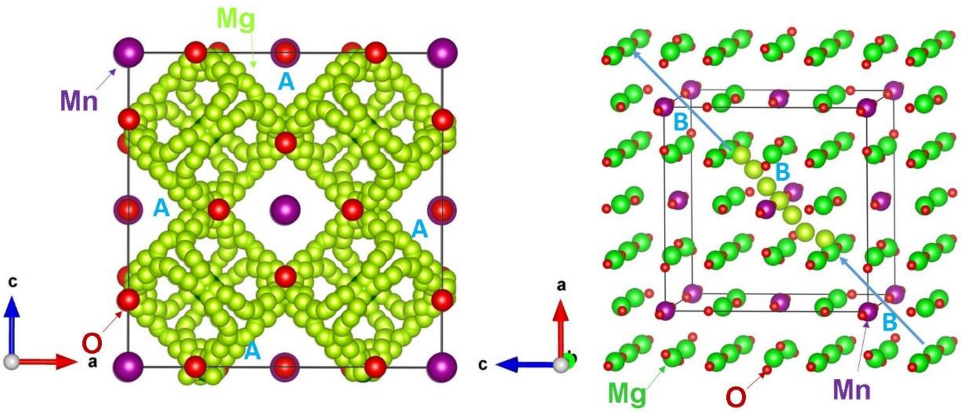

Figure 3. Possible long-range magnesium vacancy migration paths considered.

Table 2. Calculated Mg–Mg separations and activation energies for the magnesium ion diffusion between two adjacent Mg sites (refer to Figure 3).

Migration Path	Mg–Mg Separation/Å	Activation Energy/eV
A	2.98	0.82
B	5.96	3.72

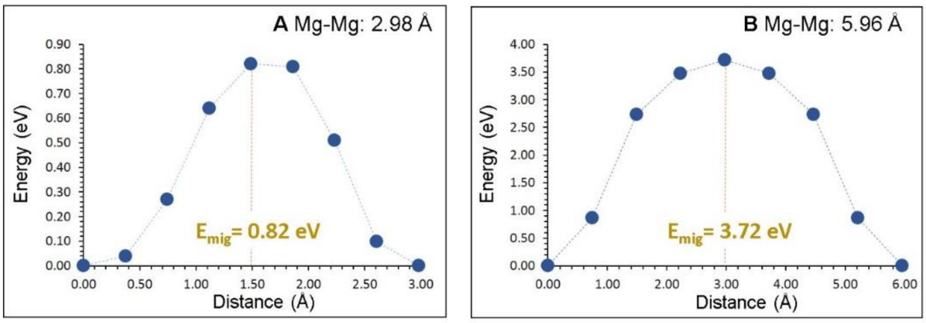

Figure 4. Energy profile diagrams of Mg vacancy hopping between two adjacent Mg sites in Mg_6MnO_8 (refer to Figure 3).

Table 3. Possible long-range Mg-ion diffusion paths and their corresponding overall activation energies.

Long-Range Path	Overall Activation Energy/eV
A→A→A→A	0.82
B→B→B→B	3.72
A→B→B→A	3.72

3.4. Dopant Substitution

Substitutional doping on Mg and Mn sites can provide useful information to the experimentalists regarding properties such as capacity and electronic properties. Here we considered a variety of aliovalent and isovalent dopants. Aliovalent substitution needed charge compensation and appropriate defects (interstitials or vacancies) introduced into the reaction equation.

Divalent dopants were first considered on the Mg site. The following reaction equation was used to calculate the solution enthalpy.

$$MO + Mg_{Mg}^{X} \rightarrow M_{Mg}^{X} + MgO \quad (9)$$

Figure 5 reports the solution enthalpies of MO (M = Fe, Co, Ni, Zn, Ca, Sr and Ba). The lowest solution enthalpy (0.01 eV) was calculated for Fe. Co, Zn and Ni also exhibit favourable solution enthalpies (<0.1 eV), suggesting that they are also promising candidates. This is because the ionic radii of those four dopants are close to each other. The calculations reveal that synthesis of $Mg_{6-x}M_xMnO_8$ (M = Fe, Co, Zn and Ni) can be carried out experimentally. Solution enthalpy increases gradually with the ionic radius from Ca^{2+} to Ba^{2+}. The solution enthalpy for Ca is 0.65 eV, meaning that doping is possible at high temperatures. As both Sr and Ba exhibit high solution enthalpies (>2.70 eV), they are highly unlikely to take place. This is due to the larger ionic radii of Sr^{2+} and Ba^{2+} compared to that of Mg^{2+} (0.72 Å).

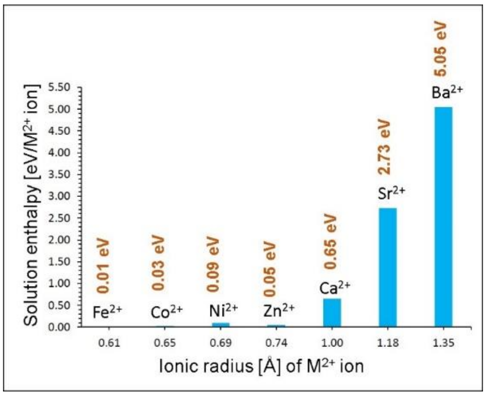

Figure 5. Enthalpy of solution of MO, (M = Fe, Co, Ni, Zn, Ca, Sr and Ba) with respect to the M^{2+} ionic radius in Mg_6MnO_8.

Next, we considered a range of trivalent dopants (Al, Ga, Fe, Sc, In, Y, Gd and La) on the Mn site. This would increase the Mg content in this material in the form of interstitials as described in Equation (10). This strategy can increase the capacity of this material providing useful information regarding promising candidate dopants.

$$M_2O_3 \ + \ 2\,Mn^{X}_{Mn} \ + \ MgO \ \rightarrow \ 2\,M'_{Mn} \ + \ Mg^{\bullet\bullet}_{i} \ + \ 2\,MnO_2 \tag{10}$$

We report the calculated solution enthalpies of M_2O_3 in Figure 6. The most favourable dopant was found to be the Ga^{3+}. The solution enthalpy for this dopant is 3.05 eV, suggesting that this process takes place under high temperatures. The possible composition would be $Mg_{6+x}Mn_{1\text{-}x}M_xO_8$ (x = 0.0–1.0). The actual composition should be determined experimentally. The Fe^{3+} is the second most stable dopant. Solution enthalpy increases with ionic radius of the dopants from Ga^{3+} to La^{3+} due to the larger ionic radii of those dopants compared to that of Mn^{4+} (0.52 Å).

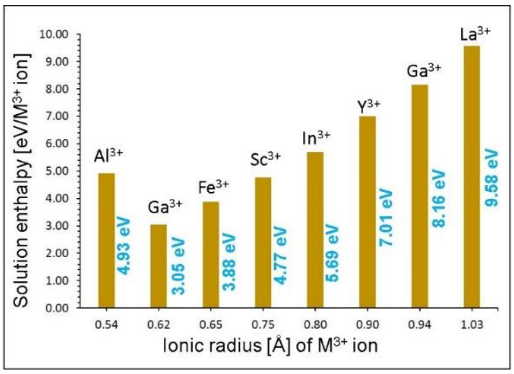

Figure 6. Enthalpy of solution of M_2O_3, (M = Al, Ga, Fe, Sc, In, Y, Ga and La) with respect to the M^{3+} ionic radius in Mg_6MnO_8.

Finally, tetravalent dopants (Si^{4+}, Ge^{4+}, Ti^{4+}, Sn^{4+}, Zr^{4+} and Ce^{4+}) were considered on the Mn site. The solution energy was calculated using the following reaction equation.

$$MO_2 + Mn^{X}_{Mn} \ \rightarrow \ M^{x}_{Mn} + \ MnO_2 \tag{11}$$

Both Si^{4+} and Ge^{4+} exhibit exothermic solution enthalpies (refer to Figure 7), suggesting that they are promising dopants. This is because the ionic radius of Mn^{4+} is closer to the ionic radii of Si^{4+} and Ge^{4+}. Experimental verification is needed for the preparation of $Mg_6Mn_{1\text{-}x}M_xO_8$. In our previous study [31], we showed that these two dopants could be exothermically substituted on the Mn site in Li_2MnO_3. All other dopants exhibit endoergic solution enthalpies. Solution enthalpy increases with ionic radius from Si^{4+} to Ce^{4+}. The solution enthalpy for Ti^{4+} is 1.19 eV. This indicates that doping is only possible at high temperatures. The least favourable dopant is Ce^{4+}. As its solution enthalpy is 7.27 eV, it is extremely difficult to carry out doping under normal conditions.

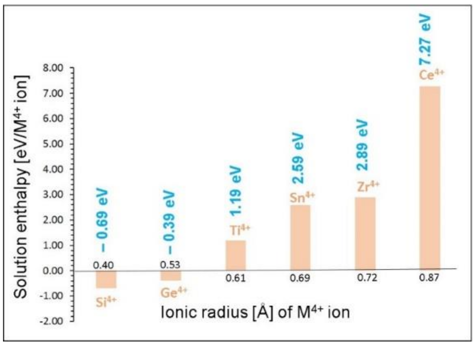

Figure 7. Enthalpy of solution of MO_2, (M = Si, Ge, Ti, Sn, Zr and Ce) with respect to the M^{4+} ionic radius in Mg_6MnO_8.

4. Conclusions

Classical pair potential simulation at the atomic scale was used to provide a detailed understanding of key issues related to defects, dopants and Mg-ion diffusion in Mg_6MnO_8. We identified that the key defect present in this material is the Mg–Mn anti-site. The second most thermodynamically dominant defect is the Mg Frenkel and this defect is present at high temperatures. The Mg-ion diffusion in this material is three-dimensional and moderate. The Ga^{3+} was identified as a promising dopant on the Mn site to increase the Mg content. Substitutional doping by the Fe^{2+} on the Mg site is favourable. Exoergic solution enthalpy was calculated for the substitution of Si^{4+} and Ge^{4+} on the Mn site, suggesting that both dopants are competitive and experimental investigation of synthesizing the composites $Mg_6Si_xMn_{1-x}O_8$, and $Mg_6Ge_xMn_{1-x}O_8$ (x = 0.0–1.0) is of worth.

Supplementary Materials: The following are available online at http://www.mdpi.com/1996-1073/12/17/3213/s1, Table S1: Interatomic potential parameters used in the atomistic simulations of Mg_6MnO_8. Table S2: Energetics of intrinsic defect process in Mg_6MnO_8: Table S3. Calculation formulas for intrinsic and extrinsic defect processes.

Author Contributions: Computation N.K.; Writing, N.K. & A.C.; Analysis N.K., A.C. & E.G.

Funding: This research was financially supported by European Union's H2020 Programme under Grant Agreement no 824072–HARVESTORE.

Acknowledgments: We acknowledge Coventry University and Imperial College London for providing computing facilities.

Conflicts of Interest: The authors declare no conflict of interest.

References

1. Xu, C.; Li, B.; Du, H.; Kang, F. Energetic Zinc Ion Chemistry: The Rechargeable Zinc Ion Battery. *Angew. Chem. Int. Ed.* **2012**, *51*, 933–935. [CrossRef]
2. Muldoon, J.; Bucur, C.B.; Gregory, T. Quest for Nonaqueous Multivalent Secondary Batteries: Magnesium and Beyond. *Chem. Rev.* **2014**, *114*, 11683–11720. [CrossRef]
3. Ponrouch, A.; Frontera, C.; Bardé, F.; Palacín, M.R. Towards a calcium-based rechargeable battery. *Nat. Mater.* **2015**, *15*, 169. [CrossRef] [PubMed]
4. Novák, P.; Imhof, R.; Haas, O. Magnesium insertion electrodes for rechargeable nonaqueous batteries—A competitive alternative to lithium? *Electrochim. Acta* **1999**, *45*, 351–367. [CrossRef]
5. Aurbach, D.; Gofer, Y.; Lu, Z.; Schechter, A.; Chusid, O.; Gizbar, H.; Cohen, Y.; Ashkenazi, V.; Moshkovich, M.; Turgeman, R.; et al. A short review on the comparison between Li battery systems and rechargeable magnesium battery technology. *J. Power Sources* **2001**, *97–98*, 28–32. [CrossRef]

6. Huie, M.M.; Bock, D.C.; Takeuchi, E.S.; Marschilok, A.C.; Takeuchi, K.J. Cathode materials for magnesium and magnesium-ion based batteries. *Coord. Chem. Rev.* **2015**, *287*, 15–27. [CrossRef]
7. Yoo, H.D.; Shterenberg, I.; Gofer, Y.; Gershinsky, G.; Pour, N.; Aurbach, D. Mg rechargeable batteries: An on-going challenge. *Energy Environ. Sci.* **2013**, *6*, 2265–2279. [CrossRef]
8. Feng, Z.; Yang, J.; NuLi, Y.; Wang, J. Sol–gel synthesis of $Mg_{1.03}Mn_{0.97}SiO_4$ and its electrochemical intercalation behavior. *J. Power Sources* **2008**, *184*, 604–609. [CrossRef]
9. Orikasa, Y.; Masese, T.; Koyama, Y.; Mori, T.; Hattori, M.; Yamamoto, K.; Okado, T.; Huang, Z.D.; Minato, T.; Tassel, C.; et al. High energy density rechargeable magnesium battery using earth-abundant and non-toxic elements. *Sci. Rep.* **2014**, *4*, 5622. [CrossRef] [PubMed]
10. NuLi, Y.; Zheng, Y.; Wang, Y.; Yang, J.; Wang, J. Electrochemical intercalation of Mg^{2+} in 3D hierarchically porous magnesium cobalt silicate and its application as an advanced cathode material in rechargeable magnesium batteries. *J. Mater. Chem.* **2011**, *21*, 12437–12443. [CrossRef]
11. Lee, S.H.; DiLeo, R.A.; Marschilok, A.C.; Takeuchi, K.J.; Takeuchi, E.S. Sol Gel Based Synthesis and Electrochemistry of Magnesium Vanadium Oxide: A Promising Cathode Material for Secondary Magnesium Ion Batteries. *ECS Electrochem. Lett.* **2014**, *3*, A87–A90. [CrossRef]
12. Huang, Z.D.; Masese, T.; Orikasa, Y.; Mori, T.; Minato, T.; Tassel, C.; Kobayashi, Y.; Kageyama, H.; Uchimoto, Y. $MgFePO_4F$ as a feasible cathode material for magnesium batteries. *J. Mater. Chem. A* **2014**, *2*, 11578–11582. [CrossRef]
13. Liu, M.; Jain, A.; Rong, Z.; Qu, X.; Canepa, P.; Malik, R.; Ceder, G.; Persson, K.A. Evaluation of sulfur spinel compounds for multivalent battery cathode applications. *Energy Environ. Sci.* **2016**, *9*, 3201–3209. [CrossRef]
14. Wan, L.F.; Perdue, B.R.; Apblett, C.A.; Prendergast, D. Mg Desolvation and Intercalation Mechanism at the Mo_6S_8 Chevrel Phase Surface. *Chem. Mater.* **2015**, *27*, 5932–5940. [CrossRef]
15. Aurbach, D.; Lu, Z.; Schechter, A.; Gofer, Y.; Gizbar, H.; Turgeman, R.; Cohen, Y.; Moshkovich, M.; Levi, E. Prototype systems for rechargeable magnesium batteries. *Nature* **2000**, *407*, 724–727. [CrossRef]
16. Gu, S.; Hsieh, C.T.; Huq, M.M.; Hsu, J.P.; Gandomi, Y.A.; Li, J. Preparation of $MgCo_2O_4$/graphite composites as cathode materials for magnesium-ion batteries. *J. Solid State Electrochem.* **2019**, *23*, 1399–1407. [CrossRef]
17. Lee, J.; Seymour, I.D.; Pell, A.J.; Dutton, S.E.; Grey, C.P. A systematic study of ^{25}Mg NMR in paramagnetic transition metal oxides: Applications to Mg-ion battery materials. *Phys. Chem. Chem. Phys.* **2017**, *19*, 613–625. [CrossRef]
18. Armstrong, A.R.; Kuganathan, N.; Islam, M.S.; Bruce, P.G. Structure and Lithium Transport Pathways in Li_2FeSiO_4 Cathodes for Lithium Batteries. *J. Am. Chem. Soc.* **2011**, *133*, 13031–13035. [CrossRef]
19. Kuganathan, N.; Iyngaran, P.; Chroneos, A. Lithium diffusion in Li_5FeO_4. *Sci. Rep.* **2018**, *8*, 5832. [CrossRef]
20. Kuganathan, N.; Ganeshalingam, S.; Chroneos, A. Defects, Dopants and Lithium Mobility in $Li_9V_3(P_2O_7)_3(PO_4)_2$. *Sci. Rep.* **2018**, *8*, 8140. [CrossRef]
21. Kuganathan, N.; Islam, M.S. Li_2MnSiO_4 Lithium Battery Material: Atomic-Scale Study of Defects, Lithium Mobility, and Trivalent Dopants. *Chem. Mater.* **2009**, *21*, 5196–5202. [CrossRef]
22. Fisher, C.A.J.; Kuganathan, N.; Islam, M.S. Defect chemistry and lithium-ion migration in polymorphs of the cathode material Li_2MnSiO_4. *J. Mater. Chem. A* **2013**, *1*, 4207–4214. [CrossRef]
23. Kuganathan, N.; Kordatos, A.; Chroneos, A. Li_2SnO_3 as a Cathode Material for Lithium-ion Batteries: Defects, Lithium Ion Diffusion and Dopants. *Sci. Rep.* **2018**, *8*, 12621. [CrossRef] [PubMed]
24. Kuganathan, N.; Chroneos, A. Defects, Dopants and Sodium Mobility in Na_2MnSiO_4. *Sci. Rep.* **2018**, *8*, 14669. [CrossRef] [PubMed]
25. Kuganathan, N.; Chroneos, A. Defects and dopant properties of $Li_3V_2(PO_4)_3$. *Sci. Rep.* **2019**, *9*, 333. [CrossRef] [PubMed]
26. Kuganathan, N.; Kordatos, A.; Chroneos, A. Defect Chemistry and Li-ion Diffusion in Li_2RuO_3. *Sci. Rep.* **2019**, *9*, 550. [CrossRef] [PubMed]
27. Kuganathan, N.; Kordatos, A.; Fitzpatrick, M.E.; Vovk, R.V.; Chroneos, A. Defect process and lithium diffusion in Li_2TiO_3. *Solid State Ion.* **2018**, *327*, 93–98. [CrossRef]
28. Kuganathan, N.; Kordatos, A.; Anurakavan, S.; Iyngaran, P.; Chroneos, A. Li_3SbO_4 lithium-ion battery material: Defects, lithium ion diffusion and tetravalent dopants. *Mater. Chem. Phys.* **2019**, *225*, 34–41. [CrossRef]
29. Kuganathan, N.; Chroneos, A. $Na_3V(PO_4)_2$ cathode material for Na ion batteries: Defects, dopants and Na diffusion. *Solid State Ion.* **2019**, *336*, 75–79. [CrossRef]

30. Kuganathan, N.; Iyngaran, P.; Vovk, R.; Chroneos, A. Defects, dopants and Mg diffusion in $MgTiO_3$. *Sci. Rep.* **2019**, *9*, 4394. [CrossRef]
31. Kuganathan, N.; Sgourou, E.N.; Panayiotatos, Y.; Chroneos, A. Defect Process, Dopant Behaviour and Li Ion Mobility in the Li_2MnO_3 Cathode Material. *Energies* **2019**, *12*, 1329. [CrossRef]
32. Kordatos, A.; Kuganathan, N.; Kelaidis, N.; Iyngaran, P.; Chroneos, A. Defects and lithium migration in Li_2CuO_2. *Sci. Rep.* **2018**, *8*, 6754. [CrossRef] [PubMed]
33. Kuganathan, N.; Kordatos, A.; Kelaidis, N.; Chroneos, A. Defects, Lithium Mobility and Tetravalent Dopants in the Li_3NbO_4 Cathode Material. *Sci. Rep.* **2019**, *9*, 2192. [CrossRef] [PubMed]
34. Kuganathan, N.; Tsoukalas, L.H.; Chroneos, A. Defects, dopants and Li-ion diffusion in Li_2SiO_3. *Solid State Ion.* **2019**, *335*, 61–66. [CrossRef]
35. Kuganathan, N.; Chroneos, A. Defect Chemistry and Na-Ion Diffusion in $Na_3Fe_2(PO_4)_3$ Cathode Material. *Materials* **2019**, *12*, 1348. [CrossRef] [PubMed]
36. Kuganathan, N.; Dark, J.; Sgourou, E.N.; Panayiotatos, Y.; Chroneos, A. Atomistic Simulations of the Defect Chemistry and Self-Diffusion of Li-ion in $LiAlO_2$. *Energies* **2019**, *12*, 2895. [CrossRef]
37. Kaushalya, R.; Iyngaran, P.; Kuganathan, N.; Chroneos, A. Defect, Diffusion and Dopant Properties of $NaNiO_2$: Atomistic Simulation Study. *Energies* **2019**, *12*, 3094. [CrossRef]
38. Gale, J.D.; Rohl, A.L. The General Utility Lattice Program (GULP). *Mol. Simul.* **2003**, *29*, 291–341. [CrossRef]
39. Gale, J.D. GULP: A computer program for the symmetry-adapted simulation of solids. *J. Chem. Soc. Faraday Trans.* **1997**, *93*, 629–637. [CrossRef]
40. Mott, N.F.; Littleton, M.J. Conduction in polar crystals. I. Electrolytic conduction in solid salts. *Trans. Faraday Soc.* **1938**, *34*, 485–499. [CrossRef]
41. Taguchi, H.; Ohta, A.; Nagao, M.; Kido, H.; Ando, H.; Tabata, K. Crystal Structure and Magnetic Properties of $(Mg_{6-x}Li_x)MnO_8$. *J. Solid State Chem.* **1996**, *124*, 220–223. [CrossRef]
42. Kröger, F.A.; Vink, H.J. Relations between the Concentrations of Imperfections in Crystalline Solids. In *Solid State Physics*; Seitz, F., Turnbull, D., Eds.; Academic Press: Cambridge, MA, USA, 1956; Volume 3, pp. 307–435.
43. Nytén, A.; Kamali, S.; Häggström, L.; Gustafsson, T.; Thomas, J.O. The lithium extraction/insertion mechanism in Li_2FeSiO_4. *J. Mater. Chem.* **2006**, *16*, 2266–2272. [CrossRef]
44. Ensling, D.; Stjerndahl, M.; Nytén, A.; Gustafsson, T.; Thomas, J.O. A comparative XPS surface study of Li_2FeSiO_4/C cycled with LiTFSI- and $LiPF_6$-based electrolytes. *J. Mater. Chem.* **2009**, *19*, 82–88. [CrossRef]
45. Liu, H.; Choe, M.J.; Enrique, R.A.; Orvañanos, B.; Zhou, L.; Liu, T.; Thornton, K.; Grey, C.P. Effects of Antisite Defects on Li Diffusion in $LiFePO_4$ Revealed by Li Isotope Exchange. *J. Phys. Chem. C* **2017**, *121*, 12025–12036. [CrossRef]
46. Devaraju, M.K.; Truong, Q.D.; Hyodo, H.; Sasaki, Y.; Honma, I. Synthesis, characterization and observation of antisite defects in $LiNiPO_4$ nanomaterials. *Sci. Rep.* **2015**, *5*, 11041. [CrossRef]
47. Politaev, V.V.; Petrenko, A.A.; Nalbandyan, V.B.; Medvedev, B.S.; Shvetsova, E.S. Crystal structure, phase relations and electrochemical properties of monoclinic Li_2MnSiO_4. *J. Solid State Chem.* **2007**, *180*, 1045–1050. [CrossRef]
48. Fisher, C.A.J.; Hart Prieto, V.M.; Islam, M.S. Lithium Battery Materials $LiMPO_4$ (M = Mn, Fe, Co, and Ni): Insights into Defect Association, Transport Mechanisms, and Doping Behavior. *Chem. Mater.* **2008**, *20*, 5907–5915. [CrossRef]
49. Nishimura, S.I.; Kobayashi, G.; Ohoyama, K.; Kanno, R.; Yashima, M.; Yamada, A. Experimental visualization of lithium diffusion in Li_xFePO_4. *Nat. Mater.* **2008**, *7*, 707. [CrossRef]
50. Peng, B.; Liang, J.; Tao, Z.; Chen, J. Magnesium nanostructures for energy storage and conversion. *J. Mater. Chem.* **2009**, *19*, 2877–2883. [CrossRef]
51. Novák, P.; Desilvestro, J. Electrochemical Insertion of Magnesium in Metal Oxides and Sulfides from Aprotic Electrolytes. *J. Electrochem. Soc.* **1993**, *140*, 140–144. [CrossRef]